Element-specific characterization of the interface magnetism in $[Co_2MnGe/Au]_n$ multilayers by x-ray resonant magnetic scattering

J. Grabis,* A. Bergmann, A. Nefedov, K. Westerholt, and H. Zabel
Ruhr-Universität Bochum, 44780 Bochum, Germany
(Received 6 December 2004; revised manuscript received 1 March 2005; published 19 July 2005)

The magnetism of the ferromagnetic half-metallic Heusler compounds at the interface with other metals, insulators, and semiconductors is a critical issue when judging the prospects for these materials to be used in future spintronic devices. We study the interface magnetism of the ferromagnetic half metal Co_2MnGe in a high-quality $[Co_2MnGe/Au]_{50}$ multilayer by x-ray resonant magnetic reflectivity using circularly polarized x-ray radiation in the energy range of the Co and Mn $L_{2,3}$ edges. An analysis of the magnetic part of the reflectivity at the superlattice Bragg peaks allows a precise determination of the magnetization profile within the Co_2MnGe layers. We find that the profile is definitely different for Mn and Co spins and asymmetric with respect to the growth direction. At room temperature nonferromagnetic interface layers exist with a thickness of about 0.45 nm at the bottom and 0.3 nm at the top of the Co_2MnGe layers. Additionally, the comparison of the nonresonant and resonant magnetic diffuse scattering reveals that the correlated structural and magnetic roughness are almost identical, the corresponding length scale being the in-plane crystallite size.

DOI: 10.1103/PhysRevB.72.024438 PACS number(s): 75.70.Cn, 85.75.−d, 78.70.Dm, 81.15.Cd

I. INTRODUCTION

Ferromagnetic metals with 100% spin polarization at the Fermi level, so-called ferromagnetic half metals, attract increasing attention in the literature, since they have the potential to play an important role in the rapidly emerging field of spintronics.[1–3] Spintronic devices are designed to control both the charge current and the spin current of the electrons in one single functional unit and will offer the realization of new concepts of data storage and data processing. Ferromagnetic half metals having only one spin direction at the Fermi level are ideally suited as electrodes in these devices, e.g., for spin injection,[4–6] spin filtering,[7] or in tunneling magnetoresistance (TMR) applications.[8]

Among the ferromagnetic half metals known in the literature there is an increasing number of Heusler alloys; these are ternary metallic compounds with the general composition A_2BX, A and B being transition metal atoms and X a nonmagnetic atom.[9] Until now theoreticians have detected about 20 different Heusler phases that are half metallic in their band structure calculations.[10–18] The most popular among them are the classical ferromagnetic half metals PtMnSb and NiMnSb,[19] so-called half Heusler compounds, since one of the A sublattices is empty; the new pseudo-ternary-phase $Co_2(Cr_{1-x}Fe_x)Al$;[18] and the phases Co_2MnSi and Co_2MnGe.[12] The latter compound is the subject of our present investigation. Co_2MnSi and Co_2MnGe are considered as excellent candidates for spintronic applications, since the volume magnetization and the ferromagnetic Curie temperatures are high (985 and 905 K, respectively) and there is good lattice matching with the GaAs semiconductor family.[20] Actually it has been shown recently that high-quality epitaxial layers of Co_2MnGe can be grown on GaAs.[21,22]

Detailed experimental investigations of the Heusler compounds in the past few years revealed how difficult it is to realize the theoretically predicted full spin polarization in thin film devices or even in single crystals. Irrespective of the experimental method applied to determine the degree of spin polarization quantitatively, whether by spin-resolved photoelectron spectroscopy,[23,24] Andreev reflection at a superconductor surface,[25] or TMR,[21] the degree of spin polarization is always definitely less than 100%. One important reason for this failure, which is often stressed by theorists, is the fact that the experiments determine the spin polarization at the surface and not in the bulk, and due to the change of symmetry at the surface the spin polarization might be lost. This can be overcome in principle by the right choice of the crystallographic direction and termination at the surface.[26]

On a more elementary basis even in bulk single crystals of the Heusler alloys the full spin polarization might be lost if the crystal structure does not coincide perfectly with the ideal $L2_1$ structure assumed in the band structure calculations. The $L2_1$ structure can be imagined to result from the metallurgical ordering of a bcc-type crystal lattice occupied by the A,B, and X atoms at random into four interpenetrating fcc sublattices occupied solely by A,B, or X atoms. The lattice parameter of the $L2_1$ unit cell doubles compared to the bcc lattice parameter upon this ordering. As usual in ordered metallic alloys, antisite disorder, e.g., an interchange of nearest-neighbor A and B atoms, frequently occurs even in well-annealed single crystals.[27,28] Theoretical model calculations taking antisite atoms into consideration show that the electronic states of these defects might fill the gap in the minority-spin band and destroy the half metallicity. In Co_2MnGe, e.g., Co atoms on the regular Mn positions create electronic states just at the Fermi energy of the minority-spin band.[29,30] In this context the interfaces between the Heusler alloys and semiconductors, insulators, or nonmagnetic metals, which typically exist in all spintronic devices, need special attention. Even in thermodynamic equilibrium it is not clear *a priori* that the ordered $L2_1$ phase is established for the first few monolayers of the film growing on the substrate. The delicate balance of the energy and entropy contributions driving the metallurgical order might be sensitively disturbed

by interactions with the substrate and epitaxial strain. Since in many spintronic applications the spin polarization for the first few monolayers is of utmost importance, this is an essential issue for a critical assessment of the perspective of the Heusler alloys to be used in future spintronic devices.

We have started a systematic study of structural and magnetic properties of multilayers of the Heusler phases Co_2MnSi, Co_2MnGe, and Co_2MnSn combined with Au, V, and Cr as interlayers and with a thickness of the Heusler compounds varied between 3 and 1 nm.[31–36] With decreasing thickness of the Heusler layers the interfaces become increasingly important for the magnetic behavior and we typically find a breakdown of the ferromagnetic saturation magnetization for a thickness below 1.5 nm for the Heusler layer.[33] This suggests that there is an interface layer of about 0.7 nm thickness which, due to site disorder and/or intermixing, is not ferromagnetic and concomitantly has a low or even vanishing spin polarization. However, macroscopic magnetization measurements and conventional structural characterization by x-ray reflectivity and large-angle x-ray diffraction cannot resolve details of the magnetization distribution within the Heusler layers.

In the present paper we want to attack this problem rigorously by applying the method of soft x-ray resonant magnetic scattering (XRMS) on a high-quality multilayer $[Co_2MnGe/Au]_{50}$. XRMS combines the depth-resolving power of conventional small-angle x-ray scattering with the element sensitivity of x-ray circular magnetic dichroism (XMCD). By observing the difference in the specular reflectivity for the two magnetization directions parallel and antiparallel to the photon helicity of circularly polarized x rays in an energy scan across the $L_{2,3}$ edge of a magnetic element, one can derive the magnetization profile of a ferromagnetic thin film. This has been demonstrated convincingly for single thin films and superlattices by other authors before.[37–39] Since in our $[Co_2MnGe/Au]_{50}$ multilayer we have two magnetic elements, we can do the analysis for Mn and Co separately. It should be mentioned here already that unfortunately in XRMS little can be learned by a mere qualitative inspection of the spectra. Only a sophisticated computer-based data analysis and fitting gives the relevant quantitative information. However, with the powerful tools available[40,41] a corresponding analysis is possible and reliable.

The subsequent central part of our paper is organized as follows. After briefly reviewing the bulk magnetic properties of $[Co_2MnGe/Au]_n$ multilayers, we report our conventional hard x-ray structural analysis of the multilayers, including off-specular (diffuse) scattering giving information about the interface morphology and the roughness correlations. Then we come to our main issue, namely, the XRMS at the $L_{2,3}$ edge of Mn and Co. Off-specular XRMS is sensitive to correlations between the chemical and magnetic roughness; this concludes the experimental section.

II. SAMPLE PREPARATION AND EXPERIMENT

The superlattice of the present study has a nominal composition $[Co_2MnGe(3\ nm)/Au(2.2\ nm)]_{50}$ and has been deposited by rf sputtering on the sapphire *a* plane at a substrate temperature of 300 °C, as described in detail elsewhere.[33]

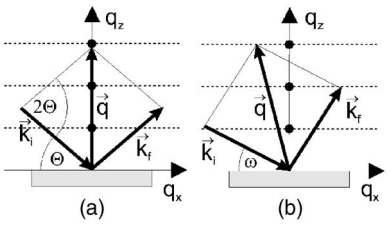

FIG. 1. Scattering geometry in reciprocal space for (a) specular reflectivity (Θ-2Θ scan, $q_x=0$) and (b) diffuse scattering (q_x scan, q_z constant). Bragg peaks in the specular reflectivity and diffuse Bragg sheets are schematically shown as dots and dotted lines, respectively.

The structural characterization was carried out using nonresonant hard x-ray scattering ($E=8$ keV) at wiggler beamline W1 at the HASYLAB (Hamburg, Germany). Two types of scans were performed as schematically depicted in Fig. 1. In the specular reflectivity (a) the scattering vector $\vec{q}$ is perpendicular to the sample surface. From these measurements information on layer thicknesses and the electron density gradient perpendicular to the surface, i.e., the structural roughness, can be obtained. In a transverse scan q_z is kept constant and q_x is varied. The scattering vector contains an in-plane component and thus yields information about correlation lengths in the sample plane.

The soft XRMS experiments were performed with the diffractometer[42] ALICE at the undulator beamlines UE56/1-PGM and UE56/2-PGM2 at BESSY II (Berlin, Germany). The diffractometer comprises a two-circle goniometer and works in horizontal scattering geometry. The vertical entrance and detector slits were set to 300 μm each, resulting in an instrument resolution of 0.14°. Circularly polarized light in the energy range of 600–900 eV was used with an energy resolution of approximately $\Delta E/E=1\times10^{-4}$. A magnetic field can be applied in the scattering plane along the sample surface either parallel or antiparallel to the photon helicity, which corresponds to the longitudinal magneto-optical Kerr effect (LMOKE) geometry. The maximum field of ±0.11 T was high enough to fully saturate the sample. The magnetic contribution to the scattered intensity was always measured by switching the magnetic field at fixed photon helicity.

The photon energies were tuned to the regions of Mn and Co $L_{2,3}$ absorption edges in order to determine the element-specific magnetic structure. The resonant magnetic scattering length is given by[43]

$$f=(\vec{\epsilon}_f^{\,*}\cdot\vec{\epsilon}_i)F^c+i(\vec{\epsilon}_f^{\,*}\times\vec{\epsilon}_i)\cdot\vec{m}F^{(1)}+(\vec{\epsilon}_f^{\,*}\cdot\vec{m})(\vec{\epsilon}_i\cdot\vec{m})F^{(2)}, \tag{1}$$

where $\vec{\epsilon}_i$ and $\vec{\epsilon}_f$ are the polarization vectors of incident and scattered x rays and $\vec{m}$ is a unit vector pointing along the magnetization direction. The scattering amplitude splits into three terms with distinct polarization dependence, where $F^c=-r_eZ+F^{(0)}$ describes the nonresonant (Thomson) and resonant charge scattering and $F^{(1)}$ and $F^{(2)}$ are the first- and second-order magnetic amplitudes, respectively. In the

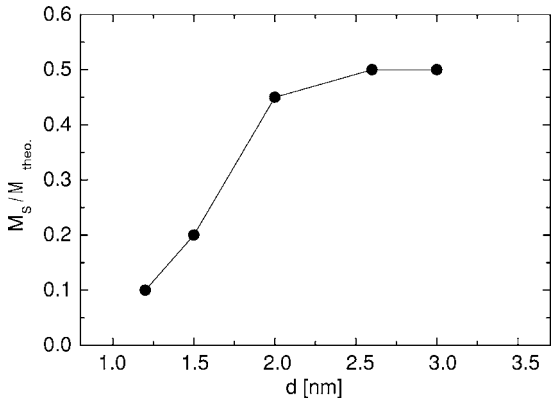

FIG. 2. Relative saturation magnetization versus the thickness of the Co_2MnGe layer for multilayers $[Co_2MnGe(d)/Au(3\ nm)]_{30}$.

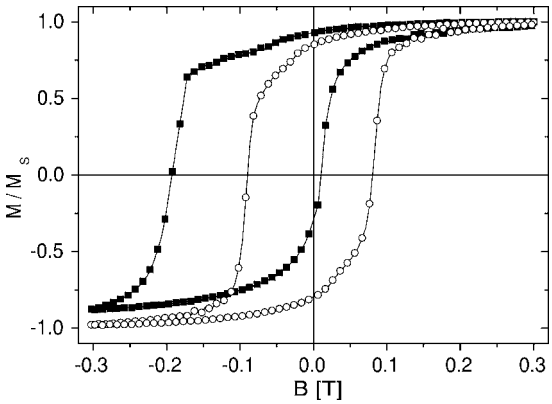

FIG. 3. Magnetic hysteresis loop measured at 4 (squares) and 14 K (circles) for a $[Co_2MnGe/Au]_{30}$ multilayer after field cooling in $B=0.02$ T (Ref. 34).

LMOKE geometry using circularly polarized light the leading magnetic contribution to scattering arises from the $F^cF^{(1)}$ interference term. Since $F^{(2)}$ is generally small compared to $F^{(1)}$ and second-order contributions do not change with a magnetization reversal, these contributions are neglected in the data analysis.

As in hard x-ray measurements, both, the specular reflectivity and diffuse scattering were measured. In order to separate the structural and magnetic contribution to the scattered intensity it is appropriate to measure the energy-dependent intensity at a fixed scattering angle 2Θ as well. All hard and soft x-ray spectra shown below have been taken at room temperature.

III. RESULTS AND DISCUSSION

A. Magnetic order of $[Co_2MnGe/Au]_n$ multilayers

In Fig. 2 we reproduce the magnetic saturation magnetization measured at 5 K via superconducting quantum interference device (SQUID) magnetometry for $[Co_2MnGe/Au]_n$ multilayers with variable layer thickness $d_{Heusler}$ of the Co_2MnGe Heusler layers and the Au layer thickness kept constant at $d_{Au}=3$ nm.[33] One sees that the saturation magnetization breaks down to very small values below 20% of the theoretical saturation magnetization corresponding to $5\mu_B$ per Co_2MnGe formula unit below a thickness of 1.5 nm. Actually the Co_2MnGe layers with $d_{Heusler}<1.5$ nm are no longer ferromagnetic but exhibit spin glass order with a spin glass freezing temperature T_G of about 20 K.[32] Above $d_{Heusler}=1.5$ nm ferromagnetic order sets in, although with a strongly reduced ferromagnetic saturation magnetization of only about 50% of the theoretical value. The ferromagnetic Curie temperatures reach about 500 K for $d_{Heusler}=3$ nm compared to 900 K for the bulk Co_2MnGe sample. Interestingly, after field cooling the ferromagnetic hysteresis loops of the $[Co_2MnGe/Au]_n$ layers exhibit a low-temperature anomaly, namely, a hysteresis loop shifted along the magnetic field axis by an exchange bias field B_{EB} (Fig. 3). Simultaneously the hysteresis loop is also shifted in the direction of positive magnetization. This is indicative of the existence of a unidirectional exchange anisotropy characterized quantitatively by the exchange bias field as discussed in detail in Ref. 44. The exchange bias shift of the hysteresis loop sets in at about $T_B=20$ K, i.e., at about the spin glass transition temperature for the very thin Co_2MnGe Heusler layers. Thus it appears natural to attribute the origin of the exchange bias field to a spin glass order of the Co_2MnGe/Au interface layers at a blocking temperature $T_B=20$ K. From this hypothesis it follows that at room temperature the interface layers should be essentially paramagnetic, i.e., contribute little to the ferromagnetic saturation magnetization. However, macroscopic magnetization measurements alone can neither really prove this hypothesis nor allow us to derive details of the magnetization profile within the Heusler layers. This is the starting point and the main aim of the present XRMS study.

B. Nonmagnetic x-ray reflectivity

In Fig. 4 the x-ray specular reflectivity of the $[Co_2MnGe/Au]_{50}$ superlattice of the present study is shown measured at a photon energy of 8048 eV. Due to the large difference in the electron densities of Au and Co_2MnGe, the contrast between the two materials is large even in nonresonant scattering. Superlattice peaks up to the ninth order are

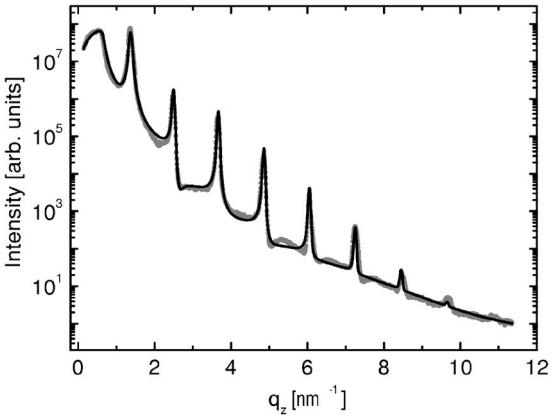

FIG. 4. Reflectivity of the Co_2MnGe/Au superlattice measured with linearly σ polarized hard x rays ($E=8048$ eV) at wiggler beamline W1 at HASYLAB, and simulation (solid line).

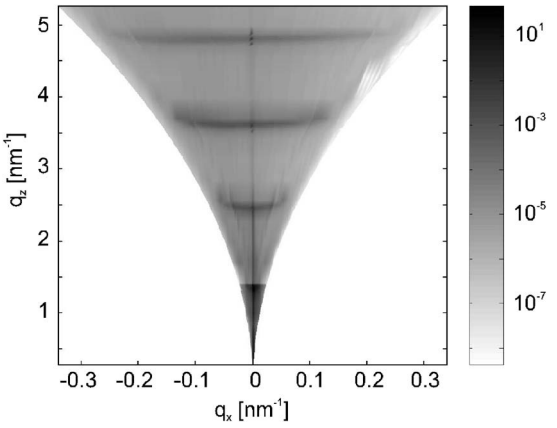

FIG. 5. q_x-q_z map. Vertically correlated roughness. The gray scale defines the intensity scale in arbitrary units.

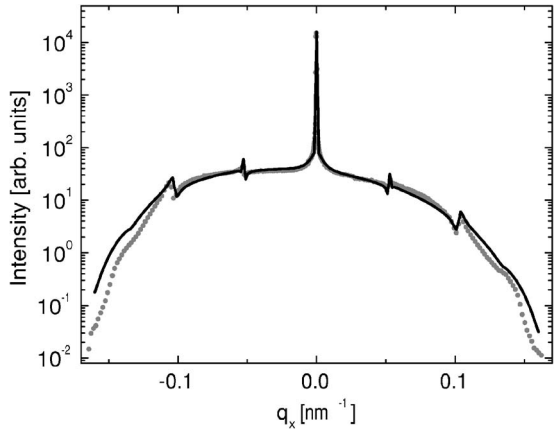

FIG. 6. Transverse q_x scan at the position of the third-order Bragg peak at $q_z=3.66$ nm^{-1} (dots) and fit within distorted-wave Born approximation (line).

visible indicating smooth interfaces. Total thickness oscillations cannot be seen since their period is smaller than the instrumental resolution. A theoretical fit to the data by the Parratt formalism[45] yields thicknesses of 2.29 and 2.93 nm for the Au and Co_2MnGe layers, respectively. While the superlattice peak positions are mainly sensitive to the bilayer thickness Λ, the relative peak intensities strongly depend on the ratio of the Co_2MnGe and Au layer thicknesses. Therefore by varying the fit parameters, the error bar to the thicknesses given above can be estimated to be 0.05 nm. The rms interface roughnesses σ of the Au and the Co_2MnGe layers resulting from the fit are $\sigma_{Au}=0.4\pm0.1$ nm and $\sigma_{Heusler}=0.3\pm0.1$ nm, respectively.

A complete reciprocal-space map of the scattered intensity is shown in Fig. 5. The vertical line of high intensity at $q_x=0$ corresponds to the specular reflectivity as shown in Fig. 4. The q_z range covers the first four superlattice peaks. The accessible q_x values are limited by the sample horizon, where either the incident or the scattered beam is parallel to the sample surface (cf. Fig. 1). Two different types of diffuse scattering appear. The first type is smeared over the whole reciprocal space and corresponds to vertically uncorrelated roughness. The second type of diffuse scattering, caused by vertically correlated roughness, appears at both sides of the superlattice peak q_z positions.

In Fig. 6 a single transverse q_x scan is shown at the q_z position of the third-order superlattice peak. Only at this position in reciprocal space does the sample horizon allow us to see the full width of diffuse scattering indicating a small in-plane roughness correlation length. The intensity of the diffuse scattering is more than two orders of magnitude smaller than the specular intensity. The additional peaks at $q_x=\pm0.05$ and ±0.1 nm^{-1} arise because either the incident or the scattered beam satisfies the Bragg condition for the first- and second-order superlattice peaks. The weak shoulder at $q_x=\pm0.14$ nm^{-1} coincides with the critical angle of Au (Yoneda wings).

The diffuse scattering spectrum can be modeled within the frame of the distorted-wave Born approximation.[46,47] The result is shown as a solid line in Fig. 6. The measured curve is not perfectly symmetric around $q_x=0$, because the sample volume probed is changing with the angle of incidence.[48] To take this asymmetry into account, the theoretical curve has been multiplied by the factor $\sin\Theta/\sin\omega$, where Θ is half of the detector angle and ω is the angle of incidence. For incident angles smaller than $\omega_0=0.4°$ it has also been taken into account that part of the incident beam does not hit the sample, giving a correction factor $\sin\omega/\sin\omega_0$. The best fit to the experimental data is obtained for a lateral roughness correlation length of $\xi_c^l=18$ nm and a vertical correlation length of $\xi_c^v=30$ nm with a Hurst parameter $h=1$,[46] where $0<h<1$ determines how smooth or jagged the surface is. The lateral correlation length can naturally be assigned to the Co_2MnGe crystallite size; the vertical correlation length is in good agreement with the thickness of coherently scattering lattice planes obtained from high-angle x-ray diffraction (see below). An additional component of diffuse scattering can be seen at small q_x values close to the specular peak. Since this q position is far away from the critical angles, it can be fitted within the kinematical approximation by a Lorentzian curve (corresponding to $h=0.5$). From the width we deduce a correlation length of 0.5 μm, which corresponds to the typical terrace length of the Al_2O_3 substrate due to its miscut angle.

It should be noted that the roughness parameters derived from the specular reflectivity in Fig. 4 also are the best parameters to fit the diffuse scattering spectra. This indicates that the rms roughness is mainly caused by topological height fluctuations. However, some interdiffusion of Au and the Heusler components Co and Mn (in the range of 0.1 to 0.2 nm) cannot be excluded due to the error bars in the fit parameters.

C. High-angle Bragg scattering

The $[Co_2MnGe/Au]_n$ superlattices grow with perfect $Co_2MnGe(110)/Au(111)$ texture out of plane. In plane they are polycrystalline.[32] In Fig. 7 we show a Bragg scan across the $Co_2MnGe(220)/Au(111)$ Bragg peak. Reflections up to the fourth order can be observed, evidencing a good coherence of the out-of-plane growth. The vertical coherence length resulting from the width of the satellite peaks is $\xi_v=30$ nm; the positions of the satellite peaks yield the same

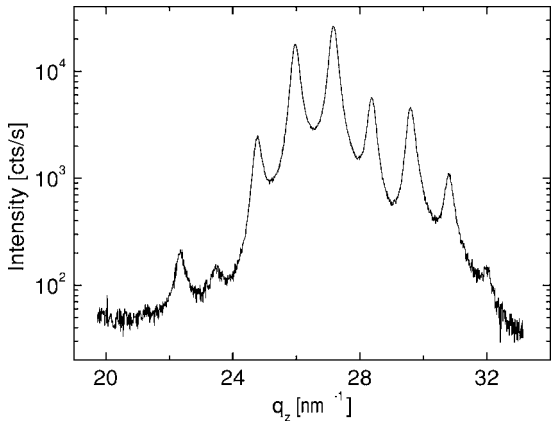

FIG. 7. Longitudinal high-angle scan of the $Co_2MnGe(220)/Au(111)$ fundamental Bragg peak.

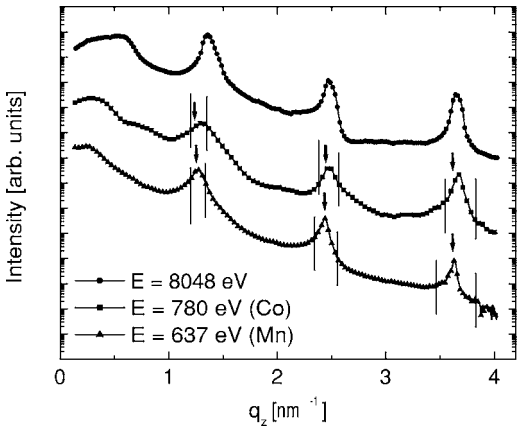

FIG. 8. Specular reflectivity measured with hard (circles) and soft x rays at the Co (squares) and Mn (triangles) L_3 edges, respectively.

superlattice period as the small-angle reflectivity above.

D. X-ray resonant magnetic reflectivity

Figure 8 compares the specular reflectivities of the $[Co_2MnGe/Au]_{50}$ superlattice up to the third-order Bragg peak, measured with hard x rays and with circularly polarized soft x rays at the Co and Mn L_3 edges in remanence, respectively. One should note that the Bragg peak positions in q_z do not exactly coincide for the different energies. This is due to the strong variation of dispersion corrections $\delta(E)$ at the Co and Mn absorption edges according to the modified Bragg law $2\Lambda \sin\Theta(1-\bar{\delta}/\sin^2\Theta)=n\lambda$, where $\bar{\delta}$ is the bilayer-averaged dispersion correction, λ is the wavelength, and n is an integer number. The peak width depends on the absorption, as can be seen in the Co reflectivity, which is measured at 780 eV, i.e., 2 eV above the Co L_3 edge. The effect is largest for small angles due to the increased photon penetration length in the sample. If the exact structural and magnetic sample composition is known, the dispersive and absorptive corrections to the refractive index can be measured from the energy-dependent peak position and width, as has been demonstrated by Mertins *et al.* for an Fe/C superlattice.[49] We have chosen the opposite approach here, i.e., with knowledge of the magneto-optical constants and precise knowledge of the chemical sample structure we determine an element-specific magnetization depth profile.

We have measured the reflected intensity of circularly polarized x rays after magnetic saturation in the directions parallel (I_+) and antiparallel (I_-) to the photon helicity at the angular position of the first three Bragg peaks. The position is indicated by the arrows in Fig. 8. The reflectivity spectra are shown in Figs. 9 and 10 for the Co and Mn $L_{2,3}$ edges, respectively.

The sum of the intensities for both magnetization directions $(I_++I_-)/2$ reflects the pure charge scattering and is independent of the magnetization of the sample. Since the momentum transfer q_z is proportional to the photon energy, the energy scan does not exactly measure the energy-dependent peak intensity but a segment of the specular reflectivity. The scanned q_z range is indicated by two vertical lines for each scan in Fig. 8. This explains the intensity increase for small and intensity drop for large energies, especially in the spectra

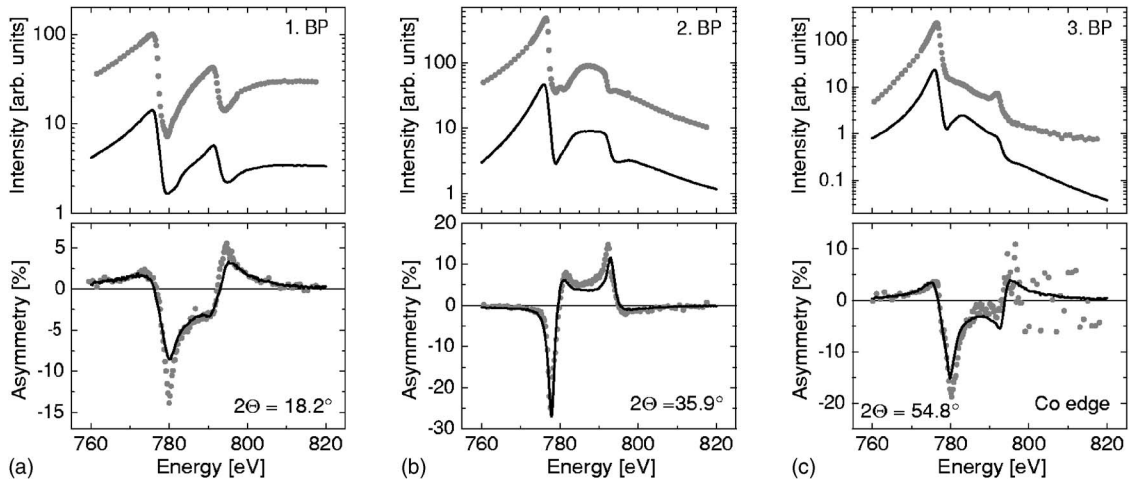

FIG. 9. Charge intensities $(I_++I_-)/2$ (top) and asymmetries $(I_+-I_-)/(I_++I_-)$ (bottom) at the first- (a), second- (b) and third- (c) order Bragg peaks at the Co $L_{2,3}$ absorption edges. The dots represent measured data; the lines are model calculations as described in the main text.

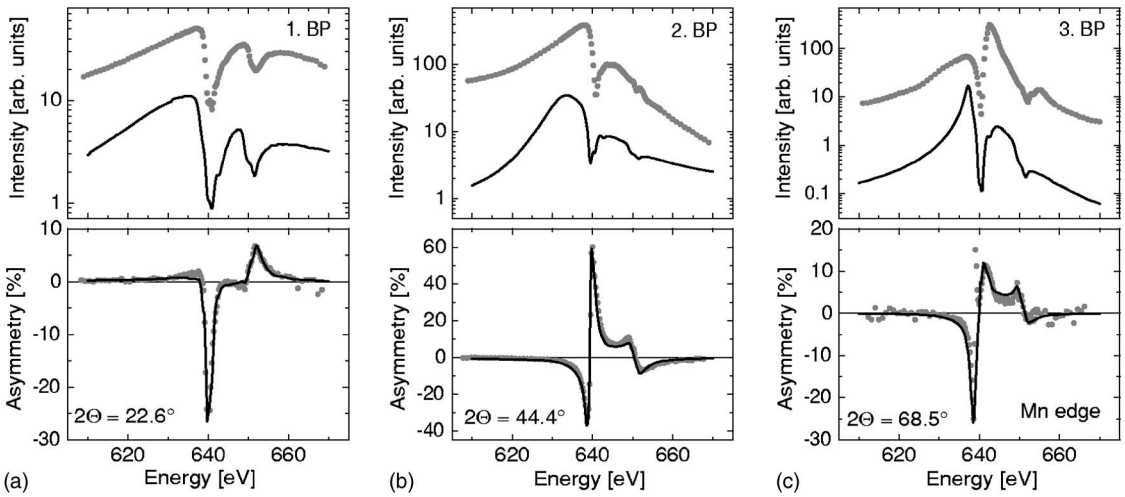

FIG. 10. Charge intensities (top) and asymmetries (bottom) at the first- (a), second- (b), and third- (c) order Bragg peaks at the Mn $L_{2,3}$ absorption edges. The dots represent measured data; the lines are model calculations as described in the main text.

of the second and third Bragg peaks. Superimposed on this line shape are the strong intensity variations due to absorption, when the energy is passing the L_3 and L_2 absorption edges of Co and Mn. Other effects of resonant scattering, such as a shift in peak position due to dispersion (see above), are difficult to assign qualitatively to specific features in the charge intensity spectra.

The magnetic contribution to the resonant scattering can best be visualized by plotting the asymmetry $(I_+ - I_-)/(I_+ + I_-)$ (second row in Figs. 9 and 10). The asymmetry of the first-order Bragg peak of Co is similar to that of the real part of the magneto-optical constant δ_m as shown in Fig. 11, with a slow increase starting approximately 10 eV below the L_3 edge, a zero crossing at the L_3 edge, a plateau between the L_3 and L_2 edges, and a second zero crossing. The asymmetry of the first-order Mn peak looks more like the corresponding imaginary part β_m of the optical constant, i.e., the XMCD signal, because the plateau between the L_3 and L_2 edges is almost absent. It is conspicuous that the overall sign of the asymmetry appears inverted for the second-order Co Bragg peak compared to the first- and third-order peaks. In the case of Mn the asymmetry of the second- and third-order Bragg peaks is inverted. This behavior already indicates on a qualitative level that the ferromagnetic magnetization introduces additional length scales which are different for Co and Mn.

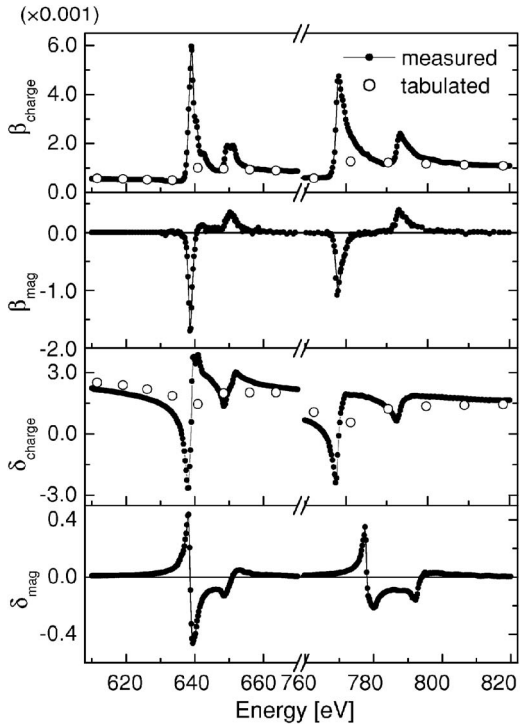

FIG. 11. Magneto-optical constants at the $L_{2,3}$ edges of Mn and Co and a comparison to the tabulated refractive index (open symbols) taken from Ref. 55.

In order to evaluate a magnetization depth profile for the $[Co_2MnGe/Au]_{50}$ superlattice from the magnetic part of the reflectivity spectra in Figs. 9 and 10, the energy-dependent intensities and asymmetries have been modeled within a magneto-optical matrix formalism developed by Zak *et al.* using the classical dielectric tensor.[40,41] Within this formalism it is possible to calculate the reflectivity for electromagnetic radiation of arbitrary incidence angle and polarization on layered structures having an arbitrary magnetization depth profile. The formalism is not limited to Bragg reflections and has been used to model magneto-optical effects at soft x-ray energies in a number of publications before.[50–52] The presence of structural and magnetic interface roughness can be included by dividing the interface into N discrete layers (typically $N=20$) with constant refractive index, which has been shown to yield the same results as the Nevot-Croce approach.[53,54]

The analysis following Ref. 40 needs the knowledge of the energy dependence of the refractive index $n=1-(\delta_c+\delta_m)+i(\beta_c+\beta_m)$ with the charge contributions δ_c and β_c and the magnetic contributions δ_m and β_m (Fig. 11). This has been determined for a Co_2MnGe film in a separate x-ray absorption experiment.[56] The imaginary part of the refractive index is directly proportional to the absorption coefficient. The real part is then calculated using the Kramers-Kronig relations.[57,58]

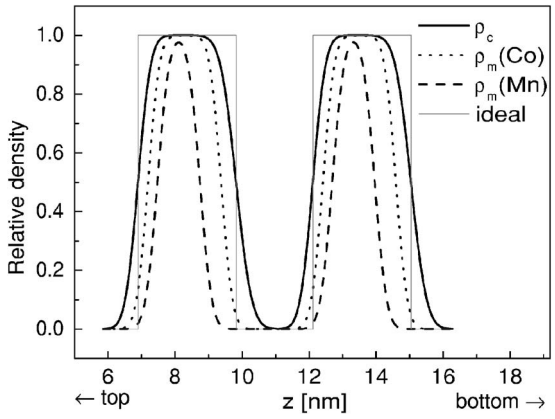

FIG. 12. Structural and magnetic depth profiles of Co and Mn as determined from model calculations (see main text).

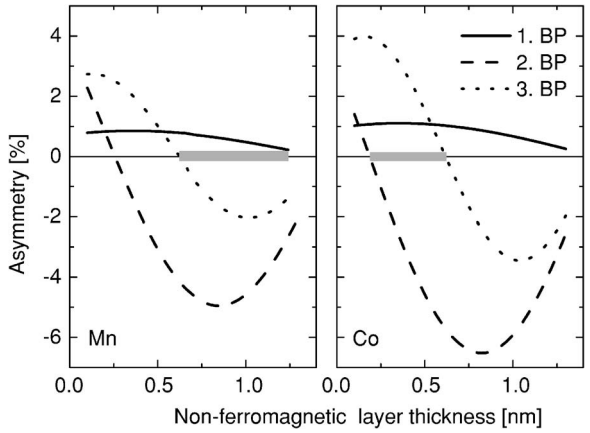

FIG. 13. Asymmetry at the first three BPs with constant energy below the Mn (left) and Co (right) L_3 edges, respectively, as a function of the nonferromagnetic layer thickness. The nonferromagnetic layers at bottom and top of the Co_2MnGe layers are assumed to be equal in thickness.

Furthermore, from the previous analysis by hard x-ray small-angle reflectivity we already have a set of well-defined parameters characterizing the chemical structure, i.e., the thickness and roughness parameters, which we keep fixed in the fit of the spectra in Figs. 9 and 10.

In the upper panels of Figs. 9 and 10 we compare the measured and the calculated charge scattering intensities $(I_+ + I_-)/2$ keeping all parameters fixed as just explained. One finds overall good agreement of the spectra. Only at the third-order Bragg peaks, where the largest q_z range is scanned, are some deviations of measured and calculated curves observed.

In the next essential step we fit the asymmetry given in the lower panels in Figs. 9 and 10 with the same set of fixed parameters, assuming a profile for the depth dependence of the ferromagnetic magnetization as discussed in detail below. We stress that the shape of the magnetic profile is the only free parameter during the fit.

We start with the plausible assumption that the magnetization profile follows exactly the chemical profile, i.e., it is given by the ideal step profile plus a smearing at the interfaces given by the chemical roughness parameter. It is found that in this case even the qualitative features of the asymmetry spectra cannot be reproduced. The first-, second-, and third-order Bragg peak asymmetries of Co and Mn then approximately have the same shape, similar to that of the first-order Bragg peak of Co. Only if nonferromagnetic interlayers at the interface of Co_2MnGe/Au are allowed can the complex features of the experimental spectra be reproduced. The best fits we obtained are shown as solid lines in the lower panels of Figs. 9 and 10 and reproduce the experimental spectra perfectly. The corresponding magnetization profiles for Co and Mn are shown in Fig. 12.

For a better comparison of charge and magnetic profiles the refractive indices are normalized according to

$$\rho_c(z) = \frac{|\delta_c(z) - \delta_{c,\mathrm{Au}}|}{|\delta_{c,\mathrm{Co_2MnGe}} - \delta_{c,\mathrm{Au}}|}, \quad \rho_m(z) = \frac{\delta_m(z)}{\delta_{m,\mathrm{Co_2MnGe}}}, \qquad (2)$$

so that $\rho(z)=1[\rho(z)=0]$ if the refractive index corresponds to the bulk Co_2MnGe (Au) value. The corresponding imaginary part $\beta_{c,m}$ has of course the same z dependence as the real part. For Co the best fit is obtained for nonferromagnetic layer thicknesses of $d_t=0.3$ nm at the top and $d_b=0.45$ nm at the bottom of the Co_2MnGe layer. For Mn the fit yields thicknesses of 0.58 and 1.08 nm for the upper and lower nonferromagnetic layers, respectively. The magnetic roughness parameters are almost identical to the structural ones—$\sigma_m=0.28$ nm for Co and Mn—and are assumed to be identical for the upper and lower magnetic interfaces.

The shape of the asymmetries at the Bragg peaks (BPs) of different order is very sensitive to the magnetization profile as shown exemplarily in Figs. 13 and 14. In the model calculation in Fig. 13 the thickness of the nonferromagnetic layer at the top and at the bottom of the Co_2MnGe layer is taken as identical and varied between 0 and 1.3 nm. The asymmetry is calculated at photon energies of 775 and 635 eV, i.e., a few eV below the Co and Mn L_3 edges. The results are very similar for both energies: While the asymmetry of the first-order Bragg peak is almost not affected by the pres-

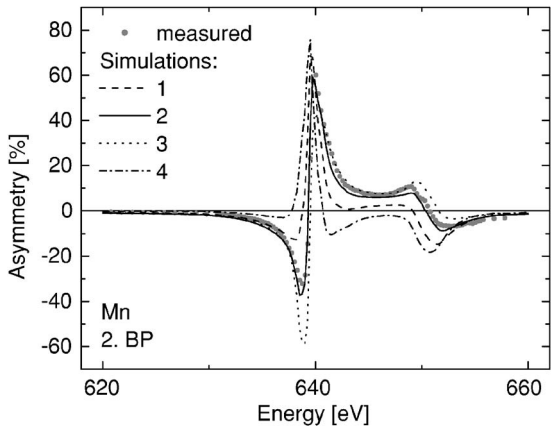

FIG. 14. Energy-dependent asymmetry at the Mn $L_{2,3}$ edge for the second-order BP. The ratio of bottom and top nonferromagnetic layer thicknesses is varied with the total thickness kept constant. (1) $d_t=d_b=0.83$ nm, (2) $d_t=0.58$ nm, $d_b=1.08$ nm, (3) $d_t=0.38$ nm, $d_b=1.30$ nm, (4) $d_t=1.08$ nm, $d_b=0.58$ nm.

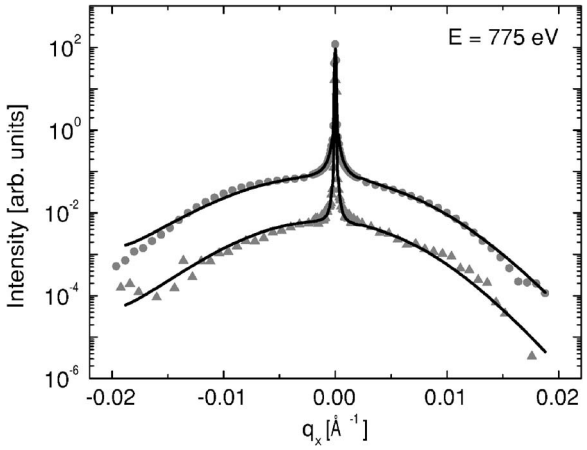

FIG. 15. Diffuse scattering at the Co edge. The measured charge (circles) and magnetic (triangles) intensities are modeled within the framework of the Born approximation (lines) as described in the main text.

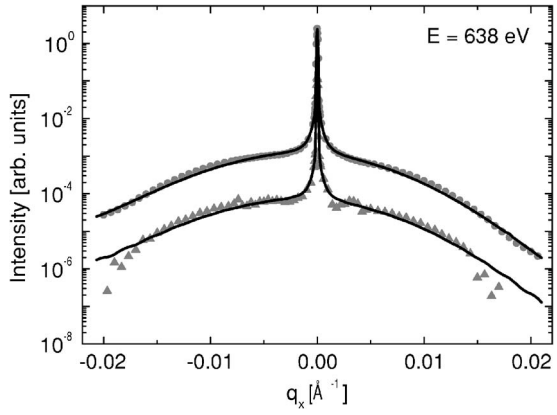

FIG. 16. Diffuse scattering at the Mn edge. The measured charge (circles) and magnetic (triangles) intensities are modeled within the framework of the Born approximation (lines) as described in the main text.

ence of nonferromagnetic interlayers, the magnitude and even the sign of the asymmetry at the second- and third-order peaks are drastically changed. The nonferromagnetic thicknesses consistent with the experimentally observed sign of the asymmetry are marked by gray bars for both elements. Thus qualitatively by just matching the sign of the asymmetry observed in the experiment, one can define that the nonferromagnetic interface layer thickness for Co must be in the limits $0.2 < d_{t,b} < 0.6$ nm; for Mn the lower limit is 0.6 nm $< d_{t,b}$.

Also the spectacular and rather puzzling asymmetry of the magnetization profile can be determined precisely. As a result of the fit, e.g., Mn possesses a nonferromagnetic layer at the bottom, whose thickness is nearly a factor of 2 larger than that at the top. In order to demonstrate the sensitivity of the spectra to the distribution between d_t and d_b, we show a model calculation for the second-order Bragg peak of Mn assuming a constant total nonferromagnetic thickness $d_{nm} = d_t + d_b = 1.63$ nm with a different distribution between d_t and d_b in Fig. 14. Only distribution 2 with $d_t = 0.58$ nm and $d_b = 1.08$ nm can reproduce the experimental spectrum. It should be stressed that this set of parameters yields the best fit to all three spectra in the lower panel of Fig. 10.

We mention that the magnetic roughness parameter is not critical in the fitting procedure. Any roughness parameter in the range $\sigma_m = 0.15$–0.35nm yields a good fit without changing the other parameters.

E. Magnetic diffuse scattering

Similar to the case of the nonmagnetic off-specular scattering, one also can study the off-specular magnetic scattering and derive information about the correlation of the magnetic roughness.[59–62] Figures 15 and 16 show transverse scans at the q_z position of the first-order superlattice peak for Co and Mn, respectively. Since the sample horizon is at larger q_x values due to the larger soft x-ray wavelengths as compared to hard x rays, the full width of diffuse scattering is already visible at the first-order Bragg peak. For each element the transverse scans were measured at an energy slightly below the L_3 edge where the absorption is relatively low and the asymmetry has a maximum [cf. Figs. 9(a) and 10(a)]. The corresponding charge $(I_+ + I_-)/2$ and magnetic $(I_+ - I_-)$ transverse scans are shown in Figs. 15 and 16. Both charge and magnetic scans exhibit the same three components as the hard x-ray transverse scan in Fig. 6: the specular peak at $q_x = 0$, a narrow component due to the substrate roughness (ξ_1, h_1), and a broad diffuse component corresponding to a short-range in-plane correlation (ξ_2, h_2). The experimental data do not show any signs of multiple reflections like Yoneda wings. Therefore the Born approximation is sufficient to describe the diffuse scattering.[60,61] The parameters for the best fits to the four transverse scans are listed in Table I.

For simplicity the vertical correlation of interfaces is assumed to be perfect in the model. This assumption is justified by the fact that the vertical correlation length as determined from the hard x-ray data is larger than the penetration depth of the soft x rays at these energies and incidence angles. The roughness parameters for the charge and the magnetization are taken from the simulation of the reflectivity. As for hard x-ray diffuse scattering the theoretical curve is multiplied by a factor $\sin\Theta/\sin\omega$ correcting the varying illumination. Due to absorption the penetration length of the soft x rays in the sample changes with ω, and the beam attenuation depends on the incidence and reflection angles. Savage *et al.* have presented a correction factor taking into account this effect,[48] which is included in the calculations of the Co and Mn transverse scans.

TABLE I. Parameters for the fit to transverse scans at both Co and Mn absorption edges.

	$\xi_1(\mu\text{m})$	h_1	ξ_2(nm)	h_2
Co, charge	0.6	0.5	24.5	1.0
Co, charge-magnetic	1.0	0.7	27.5	1.0
Mn, charge	0.6	0.5	22.5	1.0
Mn, charge-magnetic	0.7	0.5	22.0	1.0

Since the intensity difference is proportional to the charge-magnetic interference term, the existence of magnetic diffuse scattering at the Bragg peaks already indicates that the chemical and magnetic interfaces are correlated. Within the experimental error bars the magnetic interface morphology follows exactly the chemical one. This observation confirms again that the presence of nonferromagnetic layers is intrinsically correlated to chemical disorder in the sample. Both chemical and magnetic interfaces have a correlated roughness on the scale of the crystallite size.

IV. SUMMARY AND CONCLUSION

The main aim of the present paper was to derive the profile of the ferromagnetic magnetization inside a $[Co_2MnGe/Au]_n$ multilayer by the method of element-specific soft x-ray resonant magnetic scattering. In order to increase the reliability of the fitting procedure of the magnetic x-ray scattering spectra we used the structural parameters determined by conventional hard x-ray scattering as fixed input parameters.

It turned out that the asymmetry spectra at the Mn and Co $L_{2,3}$ edges have a rich internal structure which react sensitively on the magnetization profile. This sensitivity originates from the interference of waves scattered by the charge distribution and the magnetization distribution. Qualitatively the superlattice Bragg reflection of nth order depends on the nth Fourier component of the magnetization distribution and by this is sensitive to details of the magnetization profile. We stress that for a reliable determination of the magnetization profile it was essential to use a high-quality multilayer instead of a simpler Au/Co_2MnGe bi- or trilayer system, since the change of the asymmetry spectra at different superlattice Bragg peaks contains the most important information.

The resulting ferromagnetic magnetization profile within the Co_2MnGe layers gives clear evidence for the existence of nonferromagnetic interlayers, as has been hypothesized from the temperature dependence of the exchange bias field already. We find that the thickness of the nonferromagnetic interlayer is larger at the bottom than at the top of the Co_2MnGe layer and, even more remarkable, the shape of the magnetization profile determined for Mn and Co is definitely different.

The latter result seems unreasonable at the first glance, since one would expect that only one ferromagnetic layer in the core of the Co_2MnGe layer can exist. It gets a plausible explanation, however, when one takes the complex correlation between the chemical structure and the ferromagnetism of the Co_2MnGe Heusler alloys into consideration:

Metallurgically strongly disordered Co_2MnGe is nonferromagnetic and has a spin glass type of magnetic ground state.[34] Moderately disordered Co_2MnGe with, say, the Ge sublattice intact but with a large number of antisite defects in the Co and Mn sublattices, is ferromagnetic but with a reduced ferromagnetic saturation magnetization.[56] Theoretical model calculations show that a Co spin on a regular Mn position keeps its ferromagnetic spin orientation and its full moment of about $0.7\mu_B$ per Co atom.[30] Mn on a Co position, however, has an antiparallel spin orientation and a reduced moment. Thus the Mn spin is much more affected by the site disorder than the Co spin. This theoretical prediction finds corroboration in our recent XMCD measurements of a single Co_2MnGe film.[56]

The different experimental magnetization profiles for Co and Mn can then be explained by assuming a gradual transition of the metallurgical order of the Co_2MnGe film from strongly disordered (bcc type) for the first few monolayers grown on Au to well ordered ($L2_1$ type) in the core of the Co_2MnGe layer. The edge of the Co profile (see Fig. 12) indicates the onset of the ferromagnetic magnetization; the edge of the (narrower) Mn profile indicates the position inside the ferromagnetic layer where the degree of site disorder is low enough to give a resultant ferromagnetic magnetization of the Mn spins. We thus interpret the details in the Mn and Co profiles in Fig. 12 as follows.

At the bottom of the Co_2MnGe layer there is a nonferromagnetic interlayer having a thickness of 0.45 nm. Between 0.45 and 1.08 nm there is ferromagnetic order; however with a low magnetization stemming essentially from the Co spins since the Mn spins are frozen in random parallel and antiparallel orientations. Between 1.08 and 2.3 nm the chemical structure approaches the ordered $L2_1$ structure and the Mn moments are oriented ferromagnetically. Approaching the top interface with Au a metallurgically disordered layer without a ferromagnetic magnetization from the Mn spins ranging from 2.3 to 2.7 nm follows; finally, at the top of the Co_2MnGe layer again a nonferromagnetic layer of 0.3 nm thickness exists.

Translating this model into absolute values for the magnetic moments, the integration over the magnetization profiles in Fig. 12 shows that only about 45% of the Mn spins and 70% of the Co spins contributed to the ferromagnetic magnetization. The total magnetic moment measured by SQUID-based magnetometry is about 47% of the theoretical moment of $5\mu_B$ per formula unit expected if all Mn and Co spins contributed to the ferromagnetic magnetization. Referring the experimentally determined total magnetic moment to the ferromagnetically ordered Mn and Co spins within the Co_2MnGe layer only, we derive a saturation magnetic moment of $4.5\mu_B$ per formula unit which is pretty close to the theoretical full saturation moment. This indicates that in the core of the Co_2MnGe layers the magnetization is high and the chemical structure is well-ordered $L2_1$. This is remarkably different from the core layer in the thick single Heusler film,[56] where a saturation magnetic moment of approximately $3.5\mu_B$ is obtained. In the growth mode of the Co_2MnGe/Au superlattice at 300 °C one gets a higher degree of structural order for the Heusler layer than in the growth mode at 300 °C for the thick single Heusler film. The multilayer grows in a strained mode, different from the relaxed mode for the single film.

The asymmetry of the profile in the growth direction with a thicker nonferromagnetic layer at the bottom than at the top of the Co_2MnGe layer is a further point of interest which needs discussion. When deposited on the Au surface the first few monolayers of Co_2MnGe grow in a strongly disordered structure, maybe in the bcc structure with random occupation of all sublattices. Only after reaching a thickness of about 1 nm is the ordered $L2_1$ structure being established. The reason

for this could be interdiffusion of Au and Co_2MnGe; however, from the analysis of the diffuse x-ray scattering we would exclude this. The interfaces are sharp and the roughness only originates from correlated topological fluctuations. Thus the disorder seems to be induced by the Au interface, e.g., by the nonperfect lattice matching and corresponding lattice strain or by a tendency toward surface segregation of one component of the ternary Heusler compound.

The growth conditions at the other interface, namely, at the top of the Co_2MnGe layers, are very different, since here the Au film grows on a metallurgically well-ordered Heusler film. Nevertheless, strong disorder and a nonferromagnetic interlayer occur again. This disorder could be induced by the bombardment of the Heusler surface by Au atoms in the sputter discharge or again by interactions with the Au surface.

Finally, coming back to the important question concerning the applicability of the fully spin-polarized Heusler alloys in the field of spintronics, the present results indicate that the magnetism at the interfaces with other materials is a very delicate point. Nonferromagnetic interlayers as existing at the Co_2MnGe/Au interfaces can be detrimental for spintronic applications. So either one is limited to applications which can tolerate a low or vanishing spin polarization of a thin interlayer, or one must carefully search for surface combinations of the Heusler compounds and other materials without loss of ferromagnetism and chemical order.

ACKNOWLEDGMENTS

We would like to thank S. Erdt-Böhm for sample preparation and O. Seeck (HASYLAB) H.-C. Mertins, W. Mahler, and B. Zada (BESSY) for their help with beamline operation. We thank D. Lott for the helpful discussions regarding the simulation of reflectivities. This project is funded by BMBF Grant No. O3ZA6BC2 and SFB 491.

*Electronic address: johannes.grabis@ruhr-uni-bochum.de

[1] G. Prinz, Science **282**, 1660 (1998).
[2] D. Awschalom and J. Kikkawa, Phys. Today **52** (6), 33 (1999).
[3] J. Gregg, I. Petey, E. Jougelet, and C. Dennis, J. Phys. D **35**, R121 (2002).
[4] G. Schmidt, D. Ferrand, L. W. Molenkamp, A. T. Filip, and B. J. van Wees, Phys. Rev. B **62**, R4790 (2000).
[5] V. Y. Irkhin and M. I. Katsnelson, Phys. Usp. **37**, 659 (1994).
[6] W. E. Pickett, Phys. Rev. Lett. **77**, 3185 (1996).
[7] B. Dieny, J. Magn. Magn. Mater. **136**, 335 (1994).
[8] J. S. Moodera, L. R. Kinder, T. M. Wong, and R. Meservey, Phys. Rev. Lett. **74**, 3273 (1995).
[9] P. J. Webster and K. R. A. Ziebeck, in *Magnetic Properties of Metals*, edited by H. P. J. Wijn, Landolt-Börnstein New Series, Group III, Vol.19, Pt. C (Springer, Berlin, 1988), p. 75.
[10] S. Ishida, S. Fujii, S. Kashiwagi, and S. Asano, J. Phys. Soc. Jpn. **64**, 2154 (1995).
[11] S. Ishida, S. Kashiwagi, S. Fujii, and S. Asano, Physica B **210**, 140 (1995).
[12] S. Ishida, T. Masaki, S. Fujii, and S. Asano, Physica B **245**, 1 (1998).
[13] I. Galanakis, S. Ostanin, M. Alouani, H. Dreyssé, and J. M. Wills, Phys. Rev. B **61**, 4093 (2000).
[14] I. Galanakis, P. H. Dederichs, and N. Papanikolaou, Phys. Rev. B **66**, 134428 (2002).
[15] I. Galanakis, P. H. Dederichs, and N. Papanikolaou, Phys. Rev. B **66**, 174429 (2002).
[16] S. Picozzi, A. Continenza, and A. J. Freeman, Phys. Rev. B **66**, 094421 (2002).
[17] S. Picozzi, A. Continenza, and A. J. Freeman, IEEE Trans. Magn. **38**, 2895 (2002).
[18] C. Felser, *et al.*, J. Phys.: Condens. Matter **15**, 7019 (2003).
[19] R. de Groot, F. M. Mueeler, P. G. van Engen, and K. H. J. Buschow Phys. Rev. Lett. **50**, 2024 (1983).
[20] S. Picozzi, A. Continenza, and A. J. Freeman, J. Phys. Chem. Solids **64**, 1697 (2003).
[21] T. Ambrose, J. J. Krebs, and G. A. Prinz, J. Appl. Phys. **89**, 7522 (2001).
[22] F. Y. Yang, C. H. Shang, C. L. Chien, T. Ambrose, J. J. Krebs, G. A. Prinz, V. I. Nikitenko, V. S. Gornakov, A. J. Shapiro, and R. D. Shull, Phys. Rev. B **65**, 174410 (2002).
[23] D. Ristoiu, J. P. Nozieres, C. N. Borca, T. Komesu, H.-K. Jeong, and P. A. Dowben, Europhys. Lett. **49**, 624 (2000).
[24] W. Zhu, B. Sinkovic, E. Vescovo, C. Tanaka, and J. S. Moodera, Phys. Rev. B **64**, 060403(R) (2001).
[25] R. J. Soulen *et al.*, Science **282**, 85 (1998).
[26] J. P. C. M. I. Galanakis, J. Phys.: Condens. Matter **14**, 6329 (2002).
[27] M. P. Raphael, B. Ravel, Q. Huang, M. A. Willard, S. F. Cheng, B. N. Das, R. M. Stroud, K. M. Bussmann, J. H. Claassen, and V. G. Harris, Phys. Rev. B **66**, 104429 (2002).
[28] B. Ravel, M. P. Raphael, V. G. Harris, and Q. Huang, Phys. Rev. B **65**, 184431 (2002).
[29] D. Orgassa, H. Fujiwara, T. C. Schulthess, and W. H. Butler, Phys. Rev. B **60**, 13237 (1999).
[30] S. Picozzi, A. Continenza, and A. J. Freeman, Phys. Rev. B **69**, 094423 (2004).
[31] H. Bach, K. Westerholt, and U. Geiersbach, J. Cryst. Growth **237**, 2046 (2002).
[32] U. Geiersbach, A. Bergmann, and K. Westerholt, J. Magn. Magn. Mater. **240**, 546 (2002).
[33] U. Geiersbach, A. Bergmann, and K. Westerholt, Thin Solid Films **425**, 226 (2003).
[34] K. Westerholt, U. Geiersbach, and A. Bergmann, J. Magn. Magn. Mater. **257**, 239 (2003).
[35] A. Bergmann, J. Grabis, V. Leiner, M. Wolf, H. Zabel, and K. Westerholt, Superlattices Microstruct. **34**, 137 (2003).
[36] A. Nefedov, J. Grabis, A. Bergmann, K. Westerholt, and H. Zabel, Physica B **345**, 250 (2004).
[37] J. Geissler, E. Goering, M. Justen, F. Weigand, G. Schütz, J. Langer, D. Schmitz, H. Maletta, and R. Mattheis, Phys. Rev. B **65**, 020405(R) (2002).
[38] L. Seve *et al.*, Phys. Rev. B **60**, 9662 (1999).
[39] N. Jaouen *et al.*, Phys. Rev. B **66**, 134420 (2002).

[40] J. Zak, E. R. Moog, C. Liu, and S. D. Bader, Phys. Rev. B **43**, 6423 (1991).
[41] J. Zak, E. R. Moog, C. Liu, and S. D. Bader, Phys. Rev. B **46**, 5883(E) (1992).
[42] J. Grabis, A. Nefedov, and H. Zabel, Rev. Sci. Instrum. **74**, 4048 (2003).
[43] J. P. Hannon, G. T. Trammell, M. Blume, and D. Gibbs, Phys. Rev. Lett. **61**, 1245 (1988).
[44] J. Nogues and I. K. Schuller, J. Magn. Magn. Mater. **192**, 203 (1999).
[45] L. G. Parratt, Phys. Rev. **95**, 359 (1954).
[46] S. K. Sinha, E. B. Sirota, S. Garoff, and H. B. Stanley, Phys. Rev. B **38**, 2297 (1988).
[47] Z. H. Ming, A. Krol, Y. L. Soo, Y. H. Kao, J. S. Park, and K. L. Wang, Phys. Rev. B **47**, 16373 (1993).
[48] D. E. Savage, J. Kleiner, N. Schimke, Y.-H. Phang, T. Jankowski, J. Jacobs, R. Kariotis, and M. G. Lagally, J. Appl. Phys. **69**, 1411 (1991).
[49] H.-C. Mertins, O. Zaharko, A. Gaupp, F. Schäfers, D. Abramsohn, and H. Grimmer, J. Magn. Magn. Mater. **240**, 451 (2002).
[50] J. B. Kortright and S.-K. Kim, Phys. Rev. B **62**, 12216 (2000).
[51] D. Lott, Ph.D. thesis, Ludwig-Maximilians-Universität München, 2001.
[52] H.-C. Mertins, S. Valencia, D. Abramsohn, A. Gaupp, W. Gudat, and P. M. Oppeneer, Phys. Rev. B **69**, 064407 (2004).
[53] L. Nevot and P. Croce, Rev. Phys. Appl. **15**, 761 (1980).
[54] X.-L. Zhou and S.-H. Chen, Phys. Rep. **257**, 223 (1995).
[55] B. L. Henke, E. M. Gullikson, and J. C. Davis, At. Data Nucl. Data Tables **54**, 180 (1993).
[56] J. Grabis, A. Bergmann, A. Nefedov, K. Westerholt, and H. Zabel, preceding paper, Phys. Rev. B **72**, 024437 (2005).
[57] J. E. Prieto, F. Heigl, O. Krupin, G. Kaindl, and K. Starke, Phys. Rev. B **68**, 134453 (2003).
[58] K.-E. Peiponen, E. M. Vartiainen, and T. Asakura, *Dispersion, Complex Analysis and Optical Spectroscopy*, Springer Tracts in Modern Physics Vol. 147 (Springer, Berlin, 1999).
[59] J. F. MacKay, C. Teichert, D. E. Savage, and M. G. Lagally, Phys. Rev. Lett. **77**, 3925 (1996).
[60] R. M. Osgood III, S. K. Sinha, J. W. Freeland, Y. U. Idzerda, and S. D. Bader, J. Magn. Magn. Mater. **198-199**, 698 (1999).
[61] C. S. Nelson, G. Srajer, J. C. Lang, C. T. Venkataraman, S. K. Sinha, H. Hashizume, N. Ishimatsu, and N. Hosoito, Phys. Rev. B **60**, 12234 (1999).
[62] D. R. Lee, S. K. Sinha, C. S. Nelson, J. C. Lang, C. T. Venkataraman, G. Srajer, and R. M. Osgood III, Phys. Rev. B **68**, 224410 (2003).